

Numerical study of hypersonic shock wave-boundary-layer interaction flow with ablation

Mingming Ge, Ming Zeng, Peng Jin, Xiaoliang Yang, Wei Liu

owen2024@sina.cn

Abstract

Through solving the Navier-Stokes equations of thermochemical nonequilibrium flow coupled with the ablating boundary condition, the hypersonic shock wave-boundary-layer interaction flows with ablation are numerically simulated. 16 species and 29 chemical reactions are adopted in the simulation. The oxidation and sublimation of C, as well as the recombination of O catalyzed by C are considered at the wall surface. Both the compression corner flow and the boundary-layer flow with incident shock wave are calculated. The compression corner angles are 15, 18, and 24 degree, and the angles of the wedge that produce the incident shock wave are 15, 21, and 27 degree. The free stream Mach number varies from 10 to 34 and the total enthalpy from 6 to 55 MJ/kg. Both ablating and non-ablating surface conditions are used to investigate the effects of ablation on the flow properties. The flow structure, the characteristics of shock wave-boundary-layer interaction, the separation properties, and the distribution of the thermochemical properties are analyzed. The results show that the possibility of flow separation or the separation range becomes larger as the corner angle (or the angle of the wedge which produce the incident shock) rises, while smaller as the free stream Mach number is increased. As compared with the cases with low-temperature wall, the flow separation zones are larger with ablating wall or with high-temperature wall in radiation equilibrium, and this leads to further effects on the flow properties of the downstream.

Key words: hypersonic nonequilibrium flow, ablation, compression corner flow, shock wave-boundary-layer interaction

1 Introduction

The hypersonic vehicle suffers from intense aerodynamic heating when it fly at a speed of more than 7 km/s in the atmosphere. The temperature of the surface in radiation equilibrium may reach 2000K under which the internal device cannot work normally. Ablative materials are often used to absorb heat through the phase change of the material and the surface reaction between the material and the high temperature gas, and keep the inner wall of the vehicle at a suitable temperature

[1]. The ablation products ejected into the boundary layer may affect the properties of the flow field around the vehicle, such as the distributions of the temperature, the heat flux, the species mass fraction, and the ionization or radiation properties. So the study of the reentry flow field with ablation is significant. A lot of work has been carried out on the the flow field over blunt nosed bodies [2~8], and has achieved fruitful results. In this paper, the study of hypersonic flow with ablation is extended to bodies with other shape.

For the reentry vehicle and the airbreathing hypersonic vehicle, the flow in the region of control surface the engine inlet needs in-depth study because shock wave-boundary-layer interaction prevails in these regions, affecting the performance of control surface and the engine efficiency[9]. The compression corner flow and the plate boundary-layer flow with incident shock wave are typical representatives of the flow in these regions. In the compression corner flow, the boundary layer of flat plate develops gradually from the leading edge and may be interfered by the corner-generated shock. If the shock wave is strong enough, the boundary layer will be separated, and the recirculation zone will form in the corner region. The thicker boundary-layer compresses the incoming flow, resulting in a separation shock wave. The gas is compressed by the ramp near the reattachment point and a series of compression wave is produced, which coalesce into a shock wave that interact with the separation shock wave and affect the distribution of flow parameters along the compression surface. In the flow of an incident shock-generated interaction with a boundary layer, strong incident shock will lead to the separation of the boundary layer. New waves are induced, and the complex interactions will change the flow field distribution of pressure and heat flux, which may further affect the aerodynamic performance of the vehicle.

Under the condition of freestream with high-enthalpy, the wave structure and separation zone of the flowfield will be affected by the chemical reactions of the gas and the ablative wall material at high-temperature. Both the compression corner flow and the boundary-layer flow with incident shock wave corner are calculated. The compression corner angles are 15, 18, and 24 degrees, the angles of the wedge that produce the incident shock wave are 15, 21, and 27 degrees. The free stream Mach number varies from 10 to 30 and total enthalpy from 6 to 55 MJ/kg. Both ablating and non-ablating surface conditions are used to investigate the effects of ablation on the flow properties. The flow structure, the characteristics of shock-boundary-layer interaction, the separation properties, and the distribution of the thermochemical properties are analyzed.

2 Thermochemical Model

The high temperature air is composed of 10 species in the study: N₂, O₂, NO, N, O, NO₂, N₂O, O₂, N₂, e⁻. As graphite ablation occurs, the following species may also appear in the flow field: CO, CO₂, C, C₂, C₃, CN. 29 chemical reactions are considered for these 16 species. [10, 11] The two-temperature (translational/rotational and vibrational temperature) model is used to describe thermal non-equilibrium and the coupling of vibration and chemical reactions. The thermodynamic and transport properties of the gas mixture are calculated with the

method described in [10]. The surface reactions take into account the process of thermo-chemical ablation due to both oxidation and sublimation [2, 3].

Table 1 Chemical reactions in the flowfield

Number	Reaction	Number	Reaction
1	$N_2+M_1 \rightleftharpoons N+N+M_1$	16	$CO+C_2 \rightleftharpoons C_3+O$
2	$O_2+M_2 \rightleftharpoons O+O+M_2$	17	$C_3+N \rightleftharpoons CN+C_2$
3	$C_2+M_3 \rightleftharpoons C+C+M_3$	18	$C_3+C \rightleftharpoons C_2+C_2$
4	$CN+M_4 \rightleftharpoons C+N+M_4$	19	$O+N \rightleftharpoons NO^++e^-$
5	$N_2+e^- \rightleftharpoons N+N+e^-$	20	$N+N \rightleftharpoons N_2^++e^-$
6	$O+e^- \rightleftharpoons O^++e^-+e^-$	21	$CO_2+M_6 \rightleftharpoons CO+O+M_6$
7	$N+e^- \rightleftharpoons N^++e^-+e^-$	22	$CO_2+N \rightleftharpoons CN+O_2$
8	$N_2+O \rightleftharpoons NO+N$	23	$CO+NO \rightleftharpoons CO_2+N$
9	$NO+O \rightleftharpoons O_2+N$	24	$CO_2+O \rightleftharpoons CO+O_2$
10	$CO+C \rightleftharpoons C_2+O$	25	$2CO \rightleftharpoons CO_2+C$
11	$CO+O \rightleftharpoons O_2+C$	26	$N_2+CO_2 \rightleftharpoons N+N+CO_2$
12	$CO+N \rightleftharpoons CN+O$	27	$O_2+CO_2 \rightleftharpoons O+O+CO_2$
13	$N_2+C \rightleftharpoons CN+N$	28	$C_2+CO_2 \rightleftharpoons C+C+CO_2$
14	$CN+O \rightleftharpoons NO+C$	29	$CN+CO_2 \rightleftharpoons C+N+CO_2$
15	$CN+C \rightleftharpoons C_2+N$		

3 Governing Equations and Ablative Surface Boundary Conditions

3.1 Governing Equations and Numerical Methods

The governing equations for the flow field are the axisymmetric Navier-Stokes equations coupled with the vibrational and chemical kinetics, which are solved to obtain the steady state solution of the flow field. A finite difference method is used in the calculation. All inviscid terms are discretized with AUSMPW+ scheme [12]. The viscous terms are discretized with center difference scheme. The inviscid fluxes are discretized implicitly while the viscous terms explicitly. The implicit parts of the differential equations are disposed in two steps with the LU-SGS approach [13]. The details of the flow field governing equations are described in [14].

3.2 Ablative Surface Boundary Conditions and the Solution Method

To couple the flow field to the heat shield during ablation, mass balance and energy balance must be satisfied at the surface. The surface mass balance for each species is

$$-(\alpha D_s \nabla C_s \bullet \mathbf{n})_w + \dot{m}_w C_{s,w} = \dot{m}_{s,w} \quad (1)$$

where the first term on the left side is the diffusion of species, \mathbf{n} is the surface unit normal vector (away from the wall), \dot{m}_w is the total mass flux at the surface, and $\dot{m}_{s,w}$, the mass flux of species s per second, is determined from the surface thermo-chemistry [2]. There are 15 surface mass balance equations in this study with the assumption of quasi-neutral plasma.

The surface energy balance is expressed as

$$-q_w + q_{cond,w} - \alpha T_w^4 + \sum_s \dot{m}_{s,w} (h_{solid,w} - H_w) = 0 \quad (2)$$

where q_w is the heat flux to the flow from the wall, which contains both the heat conduction and the diffusive chemical heat flux, ϵT_w^4 is the re-radiation of heat into the flow, $q_{cond,w}$ is the heat flux conducting energy to the surface from the heat shield (set as zero here for the quasi-steady-state ablation), the fourth term in (2) is the removal of energy from the surface due to mass removal. To set boundary conditions for the pressure and velocity, an assumption is made that blowing occurs only normal to the body. This allows the pressure and velocity to be related through the equation of state and the conservation of mass for one-dimension.

$$(\epsilon \mathbf{V} \bullet \mathbf{n})_w = \dot{m}_w \quad (3)$$

The density of the gas in the above equation is determined from the equation of state. Moreover, the normal gradient of pressure at the surface is assumed to be zero. Then, from these surface boundary conditions (16 nonlinear equations), the surface temperature, pressure, species densities and injection velocities can be determined as part of the solution. Besides the ablative wall condition, three conditions without ablation, namely fully catalytic and non-catalytic wall at temperature of 300K, and non-catalytic wall in radiation equilibrium, are used in the flow simulation to analyze the effects of wall condition on flow properties. At full catalytic wall, the species mass fraction is set as the chemical equilibrium value at local temperature and pressure. At non-catalytic wall, the species mass fraction is determined by the zero gradient condition. The temperature of the wall in radiation equilibrium is determined by the energy balance relation $-q_w = \epsilon T_w^4$. The velocity at the wall is set as zero for the cases without ablation.

3.3 Validation of the In-house Code

The two-dimensional compression corner flow in HoldenRSS Calspan 48-inch shock tunnel [15] is calculated with the present in-house code, which can be used as a validation of the code for simulating the hypersonic flow with shock wave-boundary-layer interactions. The freestream in the shock tunnel has a Mach number of 14.1, temperature of 89K, and density of 5.27×10^{-4} kg/m³. The calculated wall pressure and heat flux are consistent with the experimental results given by [16], which is described in detail in reference [17]. As a validation of the code for simulating the hypersonic flowfield with ablation, the flow over a sphere under the reentry conditions (at speed of 10km/s and altitude of 65km) is calculated. The numerical results are in good agreement with that of [3], and the details are given in reference [8].

4 Simulation and Analysis of the Compression Corner Flow

4.1 Case Conditions and Computational Mesh

The total length of the compression corner model is 0.6096m, of which the length of the front plate is 0.3048m. The computational mesh (Figure 1) is 131×81 with 131

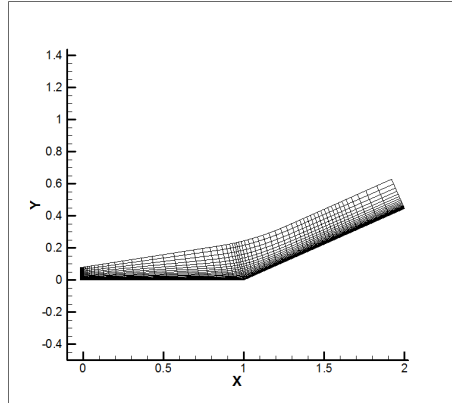


Figure 1: Computational mesh of compression corner flow

points along the surface and 81 points in the flowfield normal to the body, only half of the grid points in both directions are shown for clarity. Refined grids are used near the leading edge, the corner and the position of peak pressure. Exponential stretch is used from the wall. The first normal grid height at the wall is 6.096×10^{-5} m.

Three compression corner flows at 48 conditions are simulated. The corner angles are 15, 18, 24 degree respectively, the free stream Mach numbers are 10, 15, 20, 30, and the gas densities are those of atmosphere at altitude of 40km, 45km, 50km and 55km. The effects of the freestream conditions, the corner angle and the boundary conditions on the flow properties are analyzed. The free stream temperature is set as 300K.

4.2 Overview of the Flowfield Characteristics under Different Freestream and Wall Conditions

The calculation results show that the increase of the compression corner angle will promote the flow separation, and the increase of flow Mach number will suppress separation. The separation and reattachment point positions (SP and RP) for the corners with angle of 15 and 24 degree under 16 freestream conditions are listed In table 1 and table 2. The symbol '×' in the table represents the case without flow separation. The comparison of the flow separation characteristics under the four different wall conditions show that the results for fully catalytic and non-catalytic wall at low wall temperature are similar, while the results for the radiation equilibrium and ablative wall are similar. The flow separation zones are larger for the latter two wall conditions.

Table 1. Flow separation and reattachment position (s/L) of 15 degree compression corner

Freestream condition		300K fully catalytic		300K non-catalytic		Radiation equilibrium		Ablationm	
Altitude	Ma	SP	RP	SP	RP	SP	RP	SP	RP
40	10	0.8297	1.168	0.8297	1.168	0.7215	1.269	0.7215	1.269
	15	0.8904	1.153	0.8904	1.153	0.8056	1.251	0.8056	1.251
	20	0.9578	1.124	0.9578	1.124	0.9219	1.184	0.9219	1.200
	30	×	×	×	×	×	×	×	×
45	10	0.9353	1.124	0.9219	1.124	0.8297	1.234	0.8297	1.234
	15	0.9950	1.046	0.9950	1.046	0.9219	1.184	0.9219	1.200
	20,30	×	×	×	×	×	×	×	×
50	10	1.000	1.011	0.9950	1.011	0.9353	1.168	0.9353	1.168
	15,20,30	×	×	×	×	×	×	×	×
55	10	×	×	×	×	1.000	1.005	1.000	1.005
	15,20,30	×	×	×	×	×	×	×	×

Table 2. Flow separation and reattachment position (s/L) of 24 degree compression corner

Freestream condition		300K fully catalytic		300K non-catalytic		Radiation equilibrium		Ablationm	
Altitude	Ma	SP	RP	SP	RP	SP	RP	SP	RP
40	10	0.6287	1.167	0.6287	1.167	0.4870	1.267	0.4870	1.267
	15	0.7258	1.131	0.7258	1.131	0.6287	1.186	0.6287	1.186
	20	0.8084	1.115	0.8084	1.115	0.7551	1.149	0.7551	1.149
	30	0.8928	1.115	0.8744	1.115	0.8543	1.131	0.8543	1.149
45	10	0.5941	1.246	0.5941	1.246	0.3822	1.383	0.3822	1.415
	15	0.7551	1.167	0.7257	1.186	0.5587	1.288	0.5587	1.288
	20	0.8084	1.167	0.8084	1.167	0.7551	1.206	0.7551	1.206
	30	0.9095	1.149	0.8928	1.149	0.8543	1.186	0.8543	1.167
50	10	0.5587	1.328	0.5587	1.328	0.3822	1.493	0.3822	1.493
	15	0.6624	1.267	0.6624	1.267	0.5229	1.383	0.5229	1.383
	20	0.8323	1.206	0.8323	1.206	0.7258	1.288	0.7258	1.288
	30	0.9612	1.167	0.9246	1.186	0.8744	1.226	0.8928	1.226
55	10	0.6624	1.327	0.6624	1.327	0.5229	1.493	0.5229	1.493
	15	0.7551	1.288	0.7551	1.288	0.5587	1.288	0.5587	1.468
	20	0.8744	1.226	0.8744	1.226	0.7827	1.328	0.7827	1.328
	30	×	×	×	×	1.000	1.006	1.000	1.006

Figure 2 shows the wall pressure distribution of 24 deg compression corner at different Mach numbers and altitude of 40 km. As the Mach number increases, the flow separation zone decreases, and the peak value of the pressure on the ramp moves forward. The reason that the increase of Mach number suppresses separation has two points. On the one hand, as the Mach number increases, the shock angle of the main shock formed by the ramp decreases and the shock is closer to the surface, with the result of the decrease of the range of adverse pressure gradient. On the other hand, as the Mach number increases, the subsonic region range in the boundary layer decreases, which result in the decrease of the range for upstream propagation of the pressure gradient.

However, the influence of freestream gas density on flow separation at constant Mach number is relatively complicated. As can be seen from table 1, for 15deg compression corner flow, increasing the density will facilitate flow separation. At altitude of 40km, separation occurs at Mach number of 10, 15 and 20, only the case of Mach number of 30 is an exception; At altitude of 45km, there is separation at Mach number of 10 and 15 but not at Mach number of 20 and 30; At altitude of 50km, separation occurs only at Mach number of 10; At altitude of 55km, separation is observed only at Mach number of 10 and with wall in radiation equilibrium or with ablation. However, for 24deg compression corner flow, the effects of gas density on flow separation vary with Mach number. At high Mach number such as 30 and 20, the increase of density promotes separation; At Mach number of 15, the increase of density basically promotes separation at the low-temperature wall conditions, but postpones separation and decrease the separation zone at radiation equilibrium wall

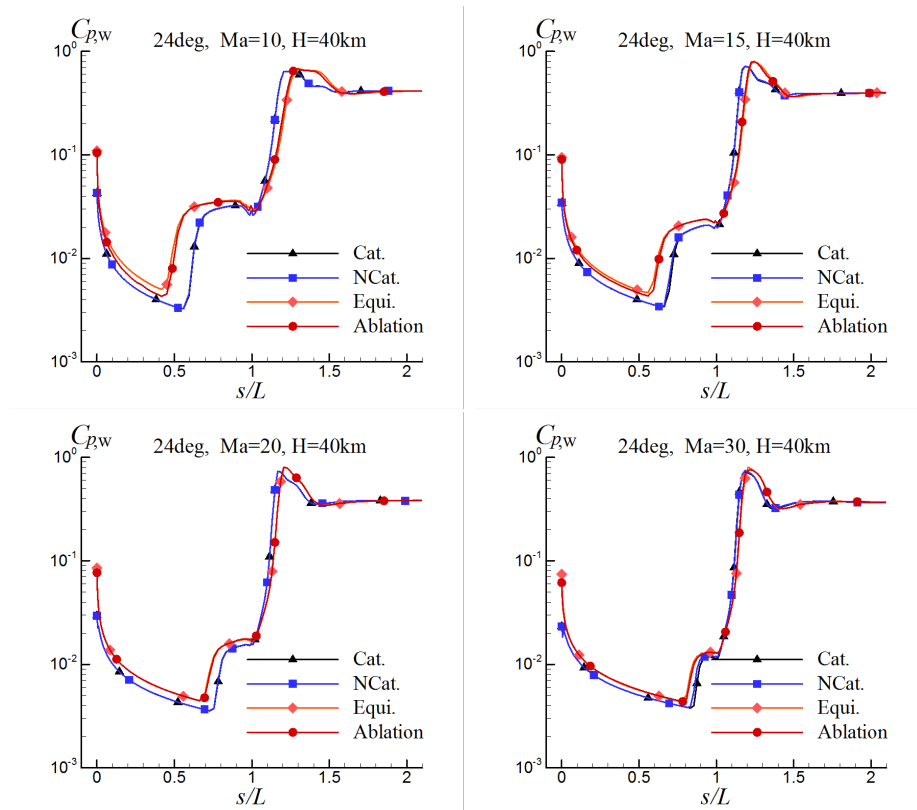


Figure 2: Surface pressure coefficient at different Mach numbers (24deg corner, $H=40\text{km}$)

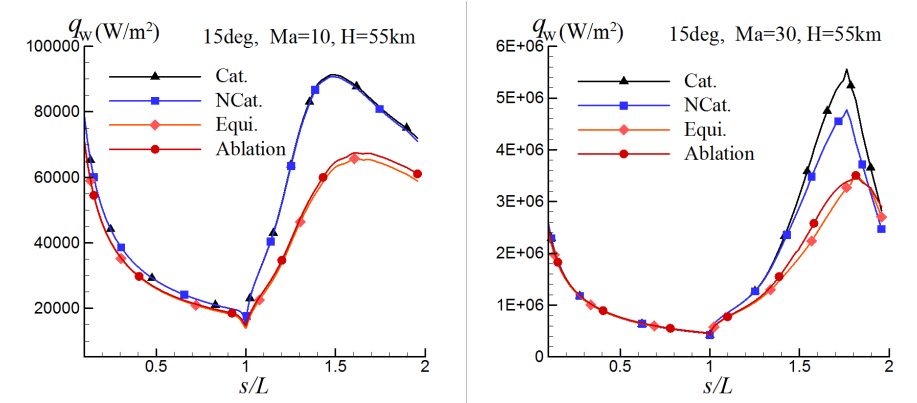


Figure 3: Surface heat flux at Mach number of 10 and 30 (15deg corner, H=40km)

and ablative wall; At lower Mach number (Ma=10), the increase of density mainly postpones separation.

4.3 Analysis of the Effects of Wall Conditions

When there is no flow separation, the wall condition mainly affects the wall heat flux, having little effects on the flowfield structure. Figure 3 shows the surface heat flux for 15deg corner at Mach number of 10 and 30 and altitude of 55 km. The heat flux values of the four different wall conditions are similar at the plate surface, but at the ramp surface, the value of radiation equilibrium wall and wall with ablation are much lower and the position of peak heat flux moves downward than that of the low temperature wall case.

As compared with the cases with low-temperature wall, the flow separation zones are larger with ablating wall or with wall in radiation equilibrium. This can be attributed to the increase of the of the boundary layer thickness induced by the increase in wall temperature. Moreover, the influence of wall conditions on the flow separation will further affect other flow properties. Take 24 deg compression corner at Mach number of 15 and altitude of 40 km and 55 km as examples, the flow field pressure distribution and the streamline in the recirculation zone for both the fully catalytic wall at 300 K and the ablative wall are given in Figure 4 and Figure 5 respectively. It can be seen that the size of the separation zone at low temperature wall is obviously smaller than that at ablative wall. This is due to the thickening of the boundary layer caused by the higher wall temperature, which affects the shape of the shock wave and its interaction with the boundary layer. With the same wall temperature, the wall catalytic properties have no significant effects on separation. The range of the separation zone under the ablative wall condition is close to that under the condition of radiation equilibrium wall without ablation.

Figure 6 shows the surface heat flux for 24 deg corner at Mach number of 15 and altitude of 40 km and 55 km. As compared with the low temperature wall case, the surface heat flux of radiation equilibrium wall and wall with ablation are fairly lower. However, the separation zone is enlarged by the higher wall temperature, and this cause the intersection of the separation shock, reattachment shock and the main shock move farther downstream, which leads to the positions of peak pressure

Numerical study of hypersonic shock wave-boundary-layer interaction flow with ablation

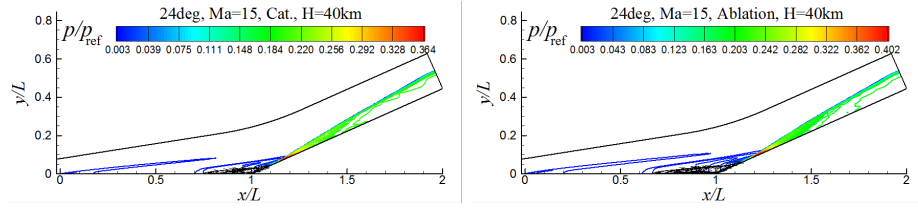


Figure 4: Pressure contour and separation zone streamline at H=40km (24deg corner, Ma=15)

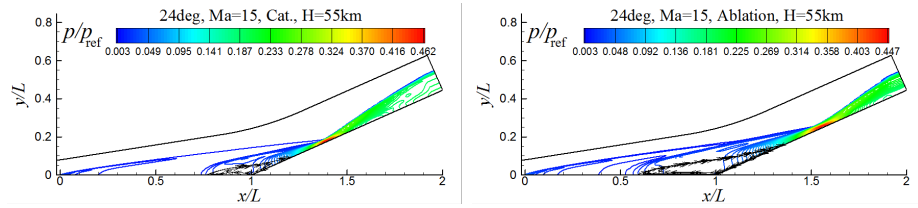


Figure 5: Pressure contour and separation zone streamline at H=55km (24deg corner, Ma=15)

and heat flux moving downstream.

Take the 24 deg corner flow at Mach number of 10 and altitude of 40 km, which has significant separation, as an example to investigate the influence of the wall conditions in detail. Figure 7 shows the normal distribution of pressure and temperature at three typical positions, namely, the start point of the ramp ($x/L=1$), the position of peak pressure and the point near the ramp end ($x/L=1.9$). The point $x/L=1$ is just near the separation chock. The thickness of the shock layer and the shock intensity under the condition of the radiation equilibrium wall and the ablative wall are obviously larger than that under the low wall temperature conditions. Moreover, the thickness for the case with radiation equilibrium wall is slightly larger than that with ablative wall. This phenomenon can be explained as follows. The increase of wall temperature leads to the thickening of the boundary layer, and therefore, enhances the leading edge shock and the separation shock, and at the same time pushes the shock away from the surface. The position of peak

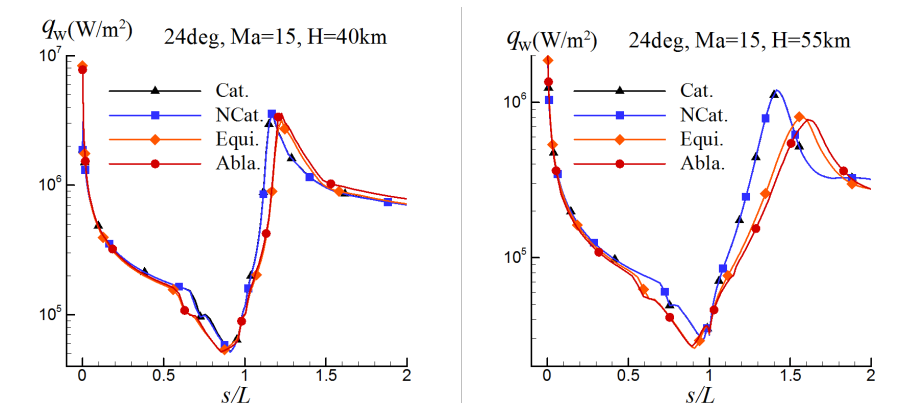


Figure 6: Surface heat flux at altitude of 40km and 55km (24deg corner, Ma=15)

pressure is just near the intersection of the main shock and the separation shock. The shock layer with high wall temperature is still thicker, and the peak values of pressure and temperature are also higher than those with low wall temperature.

4.4 Thermochemical Characteristics of the Flowfield

The 24deg compression corner flow at Mach number of 30 has the strongest shock wave, vibrational excitation, and chemical reaction. The extent of the flow nonequilibrium is enhanced with the raise of altitude and the resulting decrease of gas density. The 24 deg corner flow at Mach number of 30 and altitude of 55km is taken as an example here to analyze the thermochemical characteristics of the flowfield. The case with wall ablation is mainly discussed, and the results with other wall conditions are given only for comparison and analysis of the effects of wall condition. Figure 8 and Figure 9 show the pressure and temperature distribution of the flow field respectively, and one can see from Figure 9 that the high temperature region is near the front part of the compression surface, not coinciding with that of high pressure (Figure 8). The gas in this region has been heated first by the leading edge shock wave, then by the friction in the boundary layer, and last by the separation shock, so the temperature is even higher than the gas behind the main shock, which is heated only by the main shock from the low freestream temperature (300K).

Figure 10(a) and (b) gives the distribution of O, NO mass fraction, and Figure 10(c) gives that of the number density of electron. From comparison with Figure 9, one can see that the flow is in thermochemical non-equilibrium. The increase of the vibrational temperature and the chemical reaction lags behind the increase of translational temperature. The high translational temperature zone is located at the corner region for this case, and the translational temperature reaches its peak value at $\bar{h}, 1.16$, while the high vibrational temperature zone locates after the main shock, and the position of peak value is at $\bar{h}, 1.4$. The region of the high mass fraction of atoms is coincident with that of high vibrational temperature. There is a high temperature zone in the downstream of the main shock wave, and the vibrational excitation and chemical reaction in this high temperature zone are more significant than other regions. The peak value of mass fraction is 0.166 for O, 0.202 for NO, and up to 0.0812 for N. The peak value of NO+ mass fraction is 7.0×10^{-4} , slightly higher than that of N2+, which is 3.2×10^{-4} . The order of magnitude of mass fraction is 10^{-9} for O+, and 10^{-10} for N+. The peak value of electron number density reaches the order of 10^{14} [Figure 10(c)].

The shock layer of the case with radiation equilibrium wall and ablative wall are thicker than that with low wall temperature, which has been mentioned in 3.3, so there are also differences in the species mass fraction between the cases with high and low temperature wall. Further comparison is mainly on the species mass fraction between the cases of radiation equilibrium wall and the ablative wall. Figure 11 shows the normal distribution of the mass fraction of the main air species at the position of peak pressure and the end of the ramp under these two wall conditions. There is no significant difference in the shock layer thickness between the two conditions, and the effects of the ablation are limited to the boundary layer. The wall temperature and the surface heat flux under the ablative wall condition

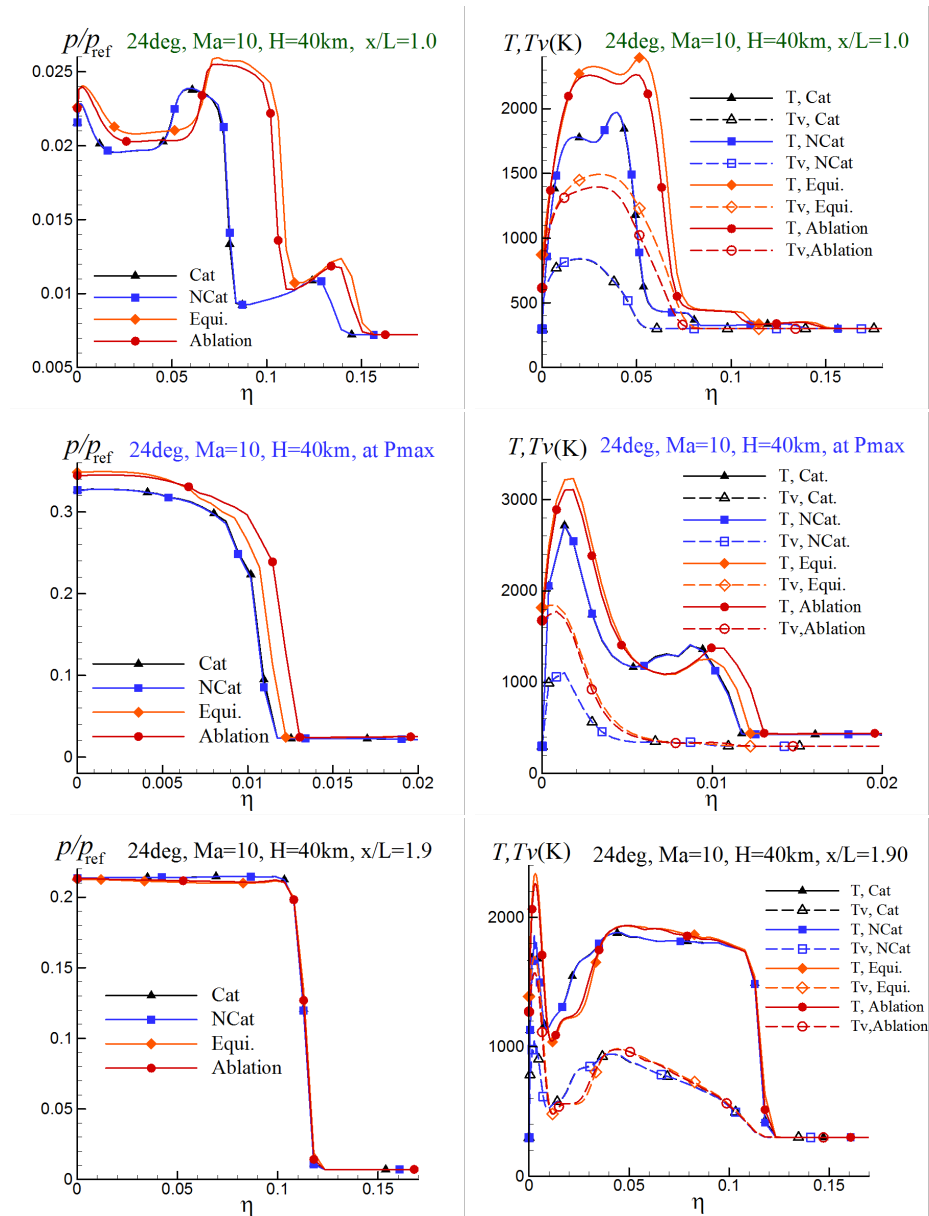


Figure 7: Normal distribution of pressure and temperature at 3 positions (24deg corner, $Ma = 10$, $H = 40\text{km}$)

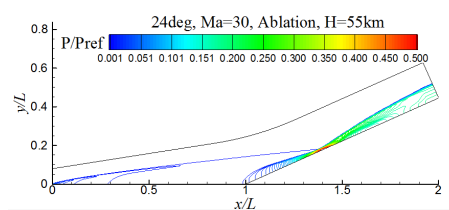


Figure 8: Pressure contour (24ocorner, $Ma=30$, $H=55\text{km}$)

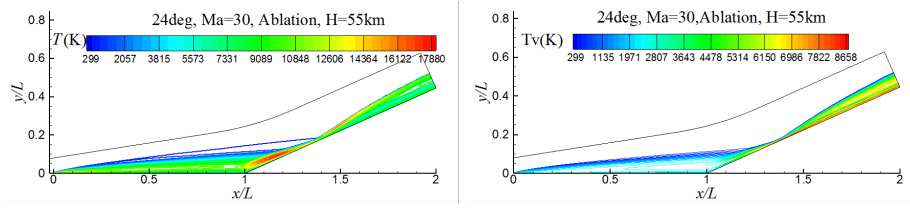


Figure 9: Temperature contours (24deg corner, Ma=30, H=55km)

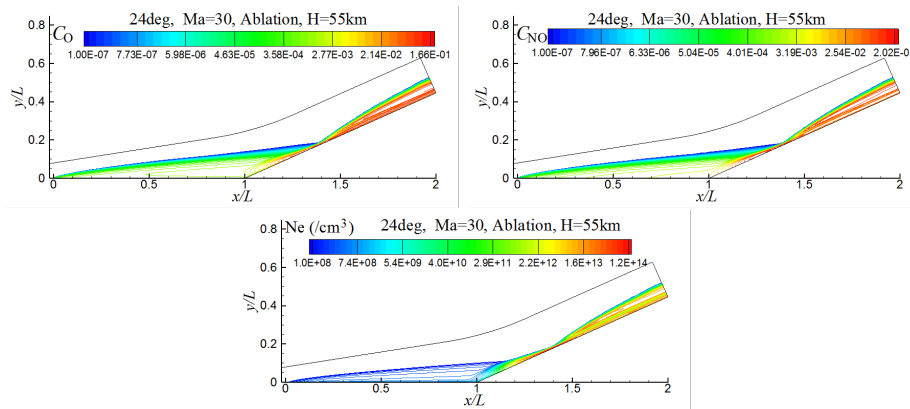


Figure 10: Contours of mass fraction of O and NO, number density of electron (24deg corner, Ma=30, H=55km)

are higher than that under radiation equilibrium wall condition. The chemical reaction and diffusion in the boundary layer are further affected by the diffusion of the ablation products into the boundary layer, which increases the mass fraction of neutral molecules (N_2 and O_2) and reduces those of the atoms (N, O) and the main ion species (NO^+ , N_2^+).

The ablation products are mainly confined to the boundary layer, and ablative species with highest mass fraction is in turn CO, C_3 , C_2 , and CN. Figure 12 shows the mass fraction distribution of CO, C_3 and CN. In addition, the peak value of mass fraction is 0.0574 for C_2 , 0.0211 for C, and in the order of 10^{-3} for CO_2 . Figure 13 shows the normal distribution of the mass fraction of the ablative species at the position of peak pressure and $x/L = 1.9$. The ablation in the plate region is rather small and the main ablation product is C_3 , which has a mass fraction of 0.01. The ablation becomes much stronger in the high pressure region after the intersection of the main shock and the reattachment shock, and the mass fraction of CO and C_3 attain the order of 0.1. The mass fraction of the ablative species continues rising downstream, and attaining their peak values near the end of the ramp.

Numerical study of hypersonic shock wave-boundary-layer interaction flow with ablation

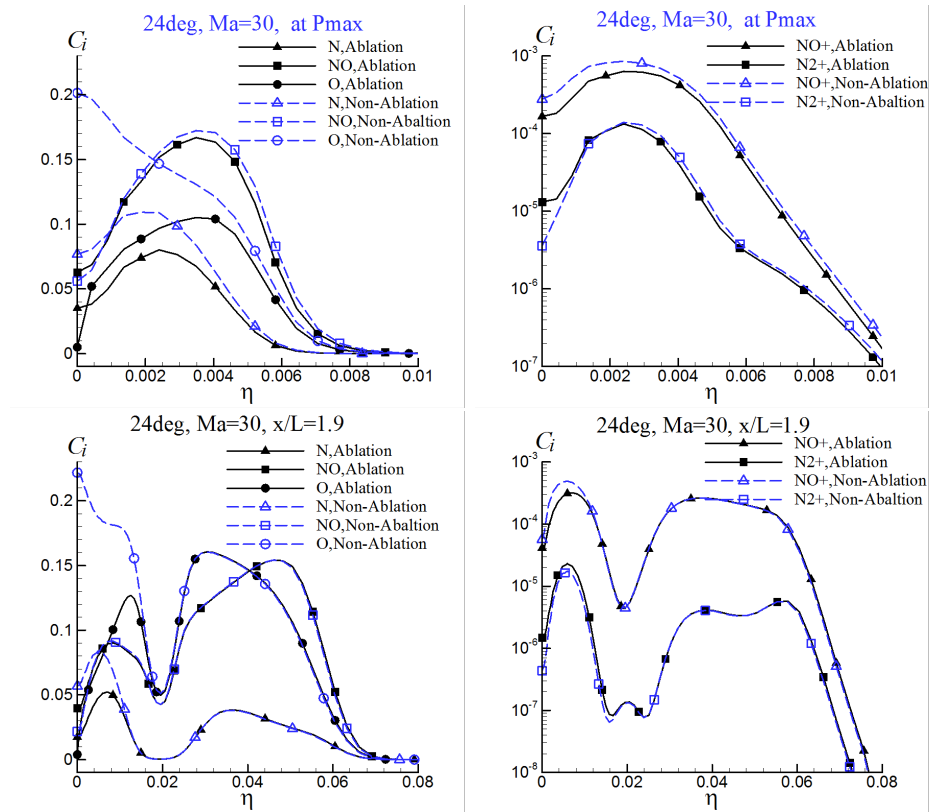


Figure 11: Normal distribution of species mass fraction at 2 positions (24deg corner, Ma=30, H=55km)

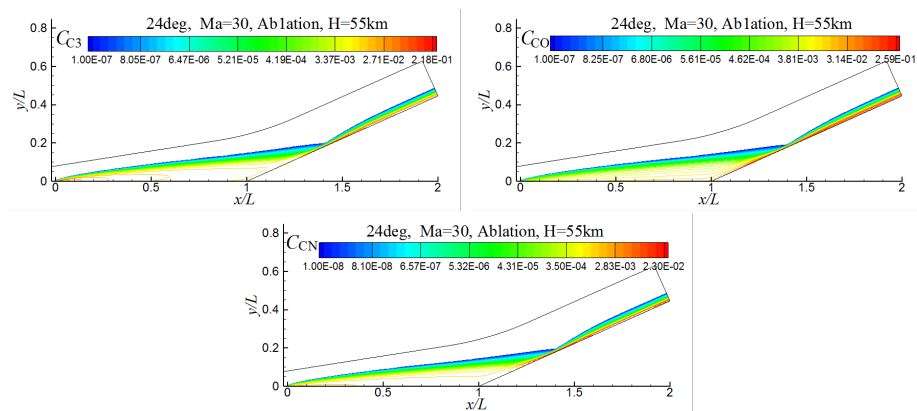


Figure 12: Mass fraction contours of the main ablation species (24deg corner, Ma = 30, H = 55km)

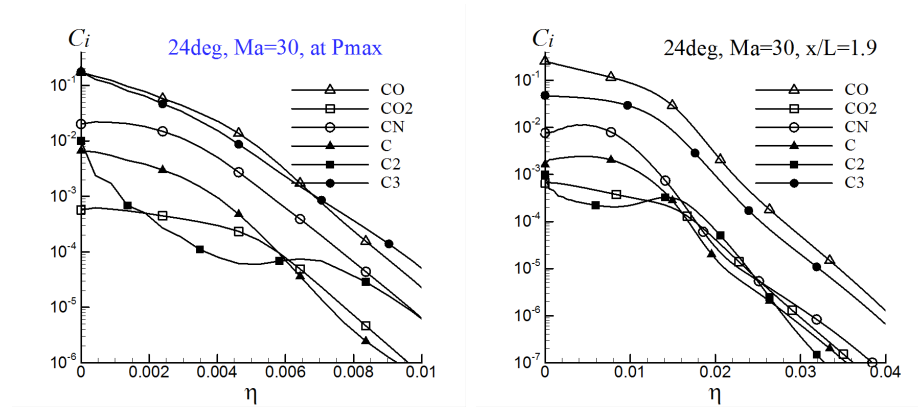


Figure 13: Normal distribution of ablation species at 2 positions (24deg corner, Ma=30, H=55km)

5 Simulation and Analysis of Boundary Layer Flow with Incident Shock

5.1 Case Conditions, Computational Boundary Conditions, and Mesh

Freestream density and temperature are set as those of the atmosphere at altitude of 60 km. Six freestream Mach number (14, 18, 22, 26, 30, 34) are selected, and the angles of the wedge which produces the incident shock are 15, 21, and 27 degree. The boundary layer flows with incident shock under a total of 18 case conditions are simulated numerically.

The computational boundary conditions of the plate flow field are set as follows (Figure 14). The left boundary of the is supersonic freestream, and the right boundary is a supersonic exit. The "1" part of the lower boundary is the wall, and the "2" part is the flow in front of the plate and set as symmetric condition. The "3" part of the upper boundary is the supersonic freestream (also the flow before shock), the "4" part is the condition after the incident shock. The "5" part can be set as a non-reflective boundary condition. The incident shock parameters are determined through the numerical simulation of the nonequilibrium flow over a wedge. The freestream condition of the wedge flow is the same as that of the plate flow, and the intensity of the incident shock under the same freestream is controlled by changing the wedge angle. The intensity of the incident "oblique shock" increases with the increase of the wedge angle and the incoming Mach number. The method of extracting the incident shock parameters from the wedge flowfield is described in [17].

Fully catalytic wall at 300K condition is set for the calculation of wedge flow. Four different wall conditions (the same as those for the corner flow) are considered in the flow over the plate. The computational mesh for the wedge flow is 121×101 . The plate length is 1m and the computational mesh is 121×101 . The first normal grid height at the wall is 10^{-4} m. Refined grids are used near the leading edge and the wall.

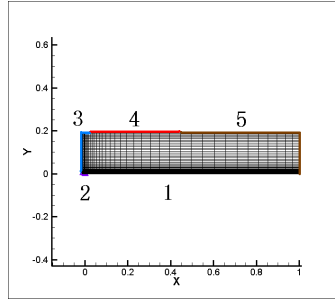


Figure 14: Boundary conditions of plate flowfield

5.2 Flowfield Characteristics under Different Freestream and Wall Conditions

Flow separations are observed for all 18 cases under the four different wall conditions. Table 3 to Table 5 give the locations of the separation and the reattachment location (x/L), in which L is the length of the plate, and x is the distance from the plate leading edge. The results show that the increase of the wedge angle promotes the separation while the increase of the Mach number delays the separation, which is similar to the case of compression corner flow. However, if the wedge angle and the wall condition keep unchanged, the reattachment location keeps stable as the Mach number changes. The separation characteristics under the fully catalytic and non-catalytic wall at low wall temperature are similar, and the results for the radiation equilibrium and ablative wall are similar. The flow separation zones are larger under the latter two wall conditions.

Table 3 Flow separation and reattachment position (x/L) for the case of 15 degree wedge

Ma	300 K fully catalytic		300K non-catalytic		Radiation equilibrium		Ablation	
	SP	RP	SP	RP	SP	RP	SP	RP
14	0.4273	0.5311	0.4273	0.5311	0.3478	0.5489	0.3478	0.5489
18	0.4611	0.5311	0.4611	0.5311	0.4108	0.5489	0.4108	0.5489
22	0.4783	0.5311	0.4783	0.5311	0.4273	0.5311	0.4273	0.5311
26	0.4783	0.5311	0.4783	0.5311	0.4611	0.5489	0.4611	0.5489
30	0.4958	0.5311	0.4958	0.5311	0.4783	0.5489	0.4783	0.5489
34	0.5134	0.5489	0.5134	0.5489	0.4958	0.5489	0.4958	0.5489

Table 4 Flow separation and reattachment position (x/L) for the case of 21 degree wedge

Ma	300 K fully catalytic		300K non-catalytic		Radiation equilibrium		Ablation	
	SP	RP	SP	RP	SP	RP	SP	RP
14	0.2394	0.3946	0.2277	0.3946	0.1657	0.4108	0.1657	0.4108
18	0.2905	0.3946	0.2905	0.3946	0.2394	0.3946	0.2394	0.3946
22	0.3184	0.3946	0.3329	0.3946	0.2771	0.3946	0.2771	0.3946
26	0.3478	0.3946	0.3478	0.3946	0.3042	0.4108	0.3042	0.4108
30	0.3478	0.3946	0.3478	0.3946	0.3184	0.3946	0.3329	0.3946
34	0.3631	0.3946	0.3631	0.3946	0.3478	0.3946	0.3478	0.3946

Table 5 Flow separation and reattachment position (x/L) for the case of 27 degree wedge

Ma	300 K fully catalytic		300K non-catalytic		Radiation equilibrium		Ablation	
	SP	RP	SP	RP	SP	RP	SP	RP
14	0.0361	0.3184	0.0361	0.3184	0.0230	0.3329	0.0230	0.3329
18	0.1173	0.3042	0.1173	0.3042	0.0859	0.3042	0.0916	0.3042
22	0.1848	0.3042	0.1750	0.3042	0.1399	0.3184	0.1567	0.3042
26	0.2164	0.3042	0.1949	0.3042	0.1657	0.3184	0.1848	0.3042
30	0.2054	0.3042	0.1847	0.3042	0.1750	0.3184	0.1848	0.3042
34	0.2277	0.3042	0.2164	0.3042	0.1949	0.3184	0.2054	0.3042

Figure 15 to Figure 17 show the flowfield pressure distribution and the streamline in the recirculation zone under different wall conditions. Figure 15 shows the results for the case of 15deg wedge and Figure 16 the 27deg wedge, both with Mach number of 14 and 34 and with ablative wall conditions. Figure 17 shows the results for the case of 27deg wedge under full catalytic wall at 300K conditions. Figure 18 shows the distribution of the wall pressure and that of the friction coefficient in the separation zone for the case of 28deg wedge and Mach number of 14.

When the freestream Mach number keeps constant, the incident shock intensity increases as the wedge angle increases. The impacts of the shock on the boundary layer flow increases, the possibility of separation and separation range becomes larger. Take the flow at Mach number of as an example, strong separation is observed for the case of 27deg wedge [see Figure 16 (a) (b)]. There are a large vortex and two small vortices in the recirculation zone. The separation for the case of 15deg wedge is much weaker, as can be seen in Figure 15 (a).

If the wedge angle keeps constant, the possibility and range of separation are reduced as the Mach number increases, which is obvious in Figure 15 and Figure 16. The reason why the increase of Mach number suppresses the separation is as follows. Although as the Mach number increases, the pressure after the incident shock rises and so does the adverse pressure gradient in the boundary layer, at the same time the kinetic energy of the gas in the boundary layer also increases. The post-shock pressure is proportional to the square of the product of the Mach number and the sine of the shock (the shock angle decreases with the increase of Mach number), but the kinetic energy of the gas in the boundary layer is proportional to the square of the freestream Mach number. Therefore, the gas ability to withstand the adverse pressure gradient may increase more than the adverse pressure gradient as the Mach number rises, therefore possibility of flow separation decreases as the Mach number increases.

There is no significant difference in the flow separation characteristics between the fully catalytic and non-catalytic wall at low wall temperature (300K), but the separation zone under radiation equilibrium wall and ablative wall condition are larger than that under low temperature wall conditions. For example, under the fully catalytic wall at 300K condition, a big and a small vortex can be seen in the recirculation zone in Figure 17 (the case at Mach number of 14 with 27deg wedge), while under the fully catalytic wall. For the ablative wall condition [Figure 16(a) and (b)] another smaller vortex can be seen above the big and the small vortex, and the separation zone is larger than that in Figure 17. The friction coefficients at the separation point are all close to -0.004 under various wall conditions, and they attain the negative peak values before the reflected shock. The peak value is about -0.022 under low temperature wall conditions and are about -0.026 under radiation equilibrium wall and ablative wall conditions (see Figure 18). The reason of the enhancement of flow separation under radiation equilibrium wall and ablative wall conditions is mainly because the thickening of the boundary layer. Figure 19 shows the wall temperature distribution for the case at Mach number of 14 with 27deg wedge. The rise in wall temperature will obviously promote separation.

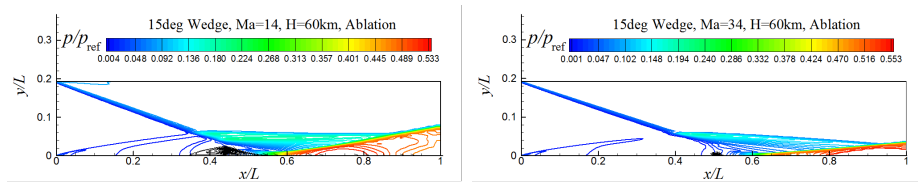


Figure 15: Pressure contour and separation zone streamline for the case of 15deg wedge (Ma= 14 and Ma=34, ablative wall)

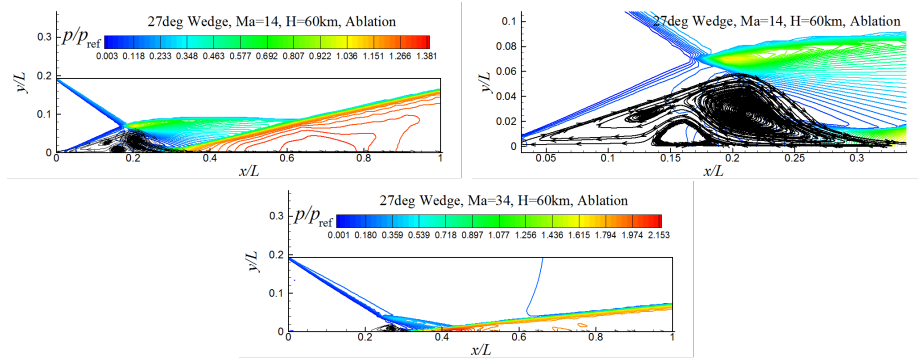


Figure 16: Pressure contour and separation zone streamline for the case of 27 deg wedge (Ma= 14 and Ma=34, ablative wall)

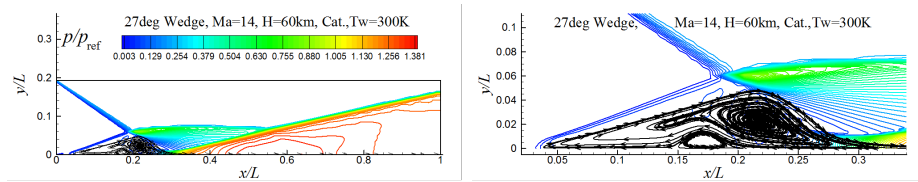


Figure 17: Pressure contour and separation zone streamline for the case of 27 deg wedge and fully catalytic wall (Ma= 14)

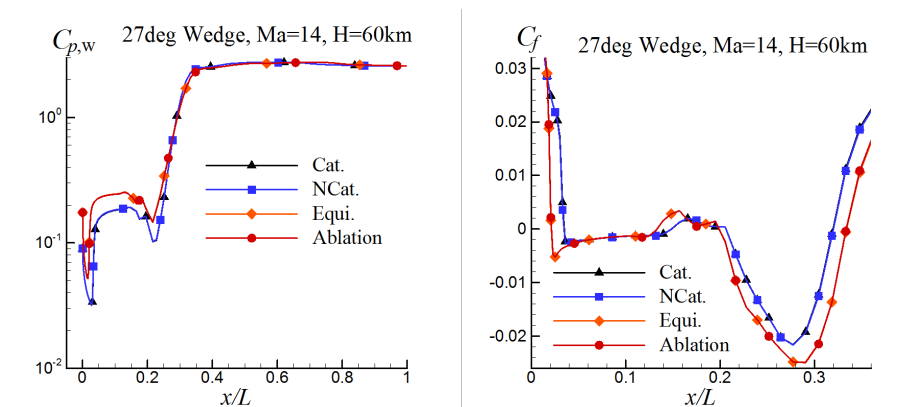


Figure 18: Surface pressure and friction coefficient (27deg wedge, Ma=14)

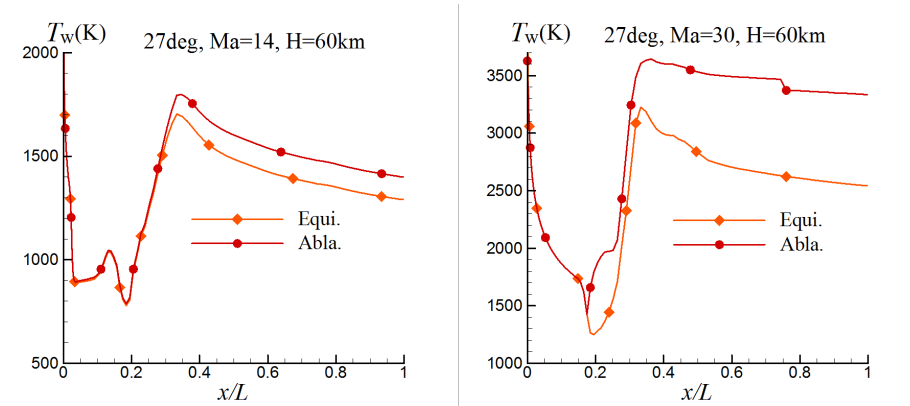


Figure 19: Surface temperature at Mach number of 14 and 30 (27deg wedge)

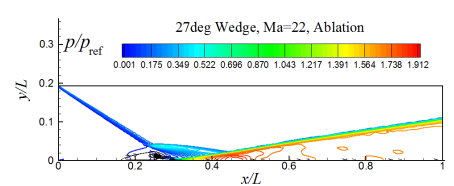


Figure 20: Pressure contour and separation zone streamline (27deg wedge, Ma= 22)

5.3 Thermochemical Characteristics of the Flowfield

The case at Mach number of 22 with 27deg wedge is taken as an example to investigate the thermochemical properties of the flowfield. Strong chemical reactions take place in the region after the incident shock (generated by the wedge), the separation and reattachment shock, and the reflected shock. Ablation at the wall is also evident. Considering that the effects of wall conditions are mainly confined to the vicinity of the wall besides the influence on the flow separation, only the results of ablation wall conditions is given here.

Figures 20 to 22 show the distributions of pressure, temperature, mass fraction of O and NO+. The flow is in thermochemical nonequilibrium, the increase of the vibrational temperature after the incident shock lags behind the increase of the translational temperature, and the chemical reaction lags more. The peak temperature appears in the vicinity of the reattachment and the reflected shock, and the peak mass fractions of atoms and ions appear near the end of the plate. This indicates that chemical reactions undergo a long relaxation distance. The vibrational temperature of the gas in the downstream of the incident shock is fairly high, and a certain amount of atoms and ions exist, which will increase further after the reflected shock.

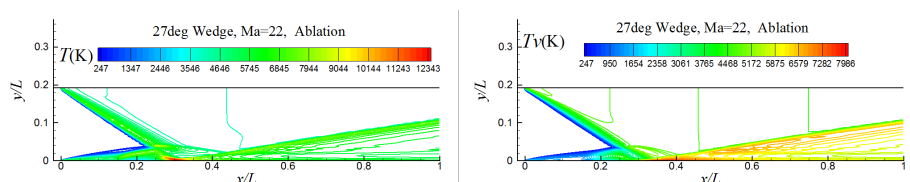


Figure 21: Temperature contours (27deg wedge, Ma= 22)

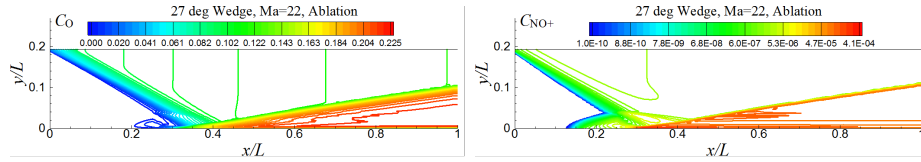


Figure 22: Mass fraction contours of O and NO+ (27deg wedge, Ma= 22)

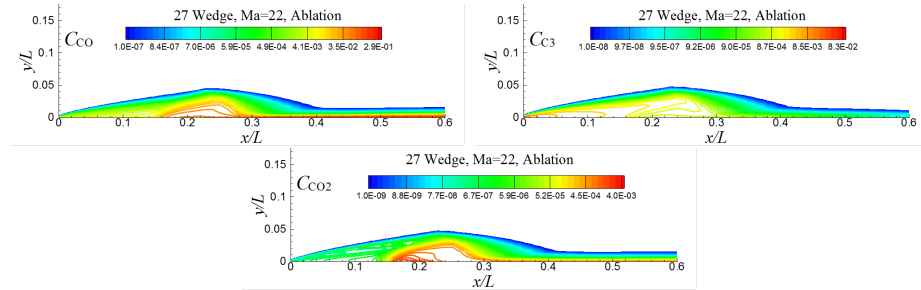


Figure 23: Mass fraction contours of main ablation species (27deg wedge, Ma= 22)

The lag of vibrational excitation and chemical reaction after the reflected shock is obviously weaker than that after the incident shock, which is closely related to the 'pre-heating' of the gas by the incident shock before the reflected shock.

The ablation products are basically confined to the recirculation zone and the boundary layer near the wall. The ablative species with highest mass fraction is in turn CO, C_3, C_2, CO_2 , and CN . The peak mass fraction of CO and CN appears near the wall after the reflected shock, while that of CO_2 occurs in the recirculation zone, because the high temperature near the wall after the reflected shock leads to further decomposition of CO_2 . The peak mass fractions of C_3 and C_2 appear after the leading edge shock in the vicinity of the leading edge, which originate from the sublimation of C . Then the amount of C_3 and C_2 decreases because of the reactions with O and N , resulting the formation of CO and CN . Figure 23 shows the mass fraction distribution of CO, C_3 , and CO_2 . Figure 24 shows the normal distribution of the mass fraction of the ablative species at the positions of peak pressure and peak temperature, and at the end of the plate. The range of the ablative species can be seen from the figure.

6 Conclusion

Taking the compression corner flow and the boundary-layer flow with incident shock wave as examples, the shock wave-boundary-layer interaction flows with ablation are numerically studied at free stream Mach number of 10 to 34 and total enthalpy from 6 to 55 MJ/kg. The compression corner angles are 15, 18, and 24 degree, and the angles of the wedge that produce the incident shock wave are 15, 21, and 27 degree. The results show:

- (1) For the compression corner flow, the possibility of flow separation and the separation range become larger as the corner angle increases, while smaller as the free stream Mach number rises.
- (2) For the boundary layer flow with incident shock wave produced by a wedge,

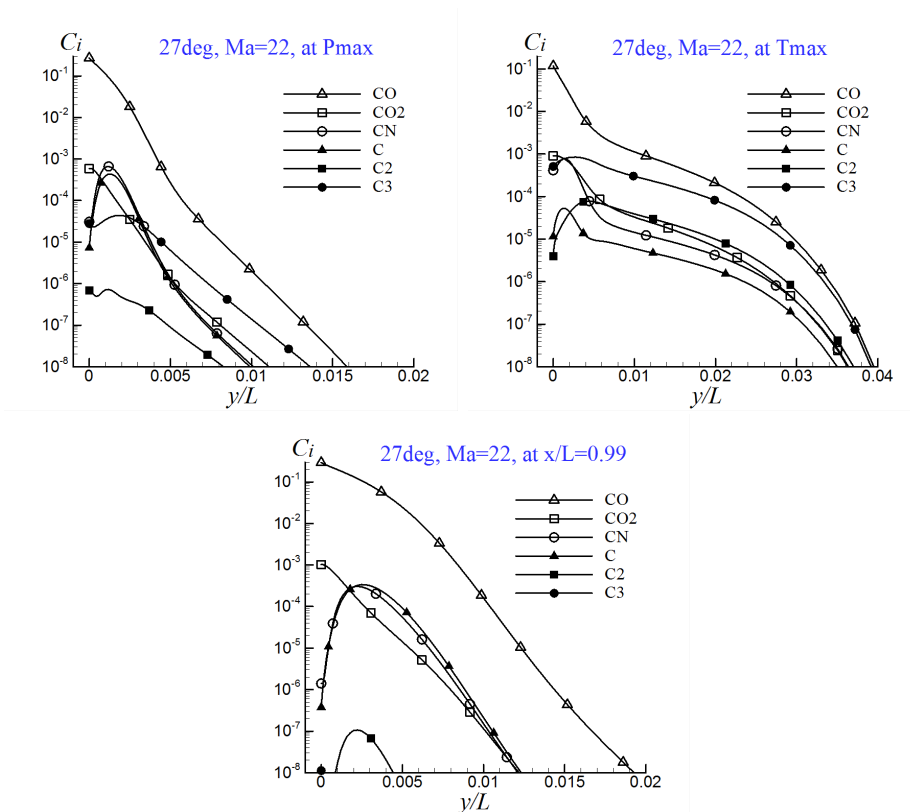


Figure 24: Normal distribution of mass fraction of main ablation species at 2 positions (27deg wedge, Ma =22)

the increase of the wedge angle and the decrease of the free stream Mach number increase the separation possibility and enlarge the separation zone.

(3) As compared with the cases with low-temperature wall, the flow separation zones are larger with ablating wall or with high-temperature wall in radiation equilibrium. For the compression corner flow, this make the positions for peak values of pressure, skin friction and heat flux move to downstream. For the boundary layer flow with incident shock wave, this also leads to further effects on the flow properties of the downstream. Therefore, the wall conditions have more evident effects on the flow properties for these shock wave-boundary-layer interaction flows than that for the flow over a sphere or a cone.

(4) As the ablation species are mainly limited to the boundary layer except for the circulation zone, the ablation effects are observed mainly in the boundary layer and the circulation zone. Out of these two regions, the flow properties for the radiation equilibrium wall condition are similar to that for the ablative wall.

Acknowledgements

The research is funded by the National Natural Science Foundation of China (11572348). and the Basic Research Foundation of National University of Defense Technology (No. ZDYJCYJ20140101).

References

- [1] LE J, GAO T, ZENG X. Reentry Physics[M]. Beijing: National Defense Industry Press, 2005. (in Chinese)
- [2] KEENAN J A, CANDLER G V. Simulation of ablation in Earth atmosphere entry[R]. AIAA 93-2789, 1993. DOI: 10.2514/6.1993-2789.
- [3] KEENAN J A, CANDLER G V. Simulation of graphite sublimation and oxidation under re-entry conditions[R]. AIAA 94-2083, 1994. DOI: 10.2514/6.1994-2083.
- [4] SUZUKI K, KUBOT H, FUJITA K, ABE T. Chemical nonequilibrium ablation analysis of MUSES-C super-orbital reentry capsule[R]. AIAA 97-2481, 1997. DOI: 10.2514/6.1997-2481.
- [5] GAO T S, DONG W Z, ZHANG Q Y. The computation and analysis for the hypersonic flow over reentry vehicles with ablation[J]. Acta Aerodynamica Sinica, 2006, 24(1): 41-45. (in Chinese) . DOI:10.3969/j.issn.0258-1825.2006.01.008
- [6] TISSERA S, TITAREV V, DRIKAKIS D. Chemically reacting flows around a double-cone including ablation effects[R]. AIAA 2010-1285, 2010. DOI: 10.2514/6.2010-1285.
- [7] BIANCHI D, NASUTI F, ONOFRI M. Aerothermodynamic analysis of reentry flows with coupled ablation. AIAA 2011-2273, 2011. DOI: 10.2514/6.2011-2273.

-
- [8] ZHANG W, ZENG M, XIAO L F, XU D. Numerical study for the effects of ablation and pyrolysis on the hypersonic reentry flow[J]. Journal of National University of Defense Technology, 2014,36(4): 41-48. (in Chinese) DOI: 10.11887/j.cn.20140400.
- [9] MALLINSON S G, GAI S L, MUDFORD N R. High enthalpy, hypersonic compression corner flow[J]. AIAA Journal, 1996, 34(6):1130-1139. DOI: 10.2514/3.13202.
- [10] PARK C, JAFFE R L, PARTRIDGE H. Chemical-kinetic parameters of hypersonic Earth entry[J]. Journal of Thermophysics and Heat Transfer, 2001, 15(1):76-90. DOI: 10.2514/2.6582.
- [11] BLOTTNER F G. Prediction of electron density in the boundary layer on entry vehicles with ablation[R]. N71-21113, 1971.
- [12] KIM K H, KIM C, RHO O H. Accurate computations of hypersonic flows using AUSMPW+ scheme and shock-aligned grid technique[R]. AIAA 98-2442, 1998. DOI: 10.2514/6.1998-2442.
- [13] STOLL P, GERLINGER P, BRUGGERMANN D. Domain decomposition for an implicit LU-SGS scheme using overlapping grids[R]. AIAA 97-0770, 1997. DOI: 10.2514/6.1997-0770.
- [14] ZENG M. Numerical rebuilding of free-stream measurement and analysis of nonequilibrium effects in high-enthalpy tunnel. [Ph D Thesis]. Beijing: Institute of Mechanics, CAS. 2007. (in Chinese)
- [15] HOLDEN M S, MOSELLE J. Theoretical and experimental studies of the shock wave-boundary layer Interaction on compression surfaces in hypersonic flow.[R]. ARL 70-0002, 1970.
- [16] RUDY D H, THOMAS J L, KUMAR A. Computation of laminar viscous-inviscid interactions in high-speed internal flows[R]. N91-21087, 1991.
- [17] WANG D F. Study of hypersonic viscous interaction including high-temperature gas effects [Master of Engineering Thesis]. Chasha: National University of Defense Technology. 2011. (in Chinese)
- [18] BABINSKY H, HARVEY, J K. Shock Wave-Boundary-Layer Interactions[M].Cambridge University Press.2011

MingMing Ge, Changsha , China

Ming Zeng, Changsha , China

Ping Jing, Changsha , China

XiaoLiang Yang, Changsha , China

Wei Liu, Changsha , China